

Article

An Extended Quasi–Analytical Algorithm for Retrieving Absorption Coefficient Using 510–620 nm Bands from OLCI and MERIS Satellite Data

Liangliang Shi ¹, Zhihua Mao ^{2,*} , Yiwei Zhang ² , Zheng Wang ³ and Qianguang Tu ¹

¹ School of Surveying and Municipal Engineering, Zhejiang University of Water Resources and Electric Power, Hangzhou 310018, China; shill@zjweu.edu.cn (L.S.); tuqg@zjweu.edu.cn (Q.T.)

² State Key Laboratory of Satellite Ocean Environment Dynamics, Second Institute of Oceanography, Ministry of Natural Resources, Hangzhou 310012, China; zhangyw@sio.org.cn

³ Institute of Geographical Science, Henan Academy of Science, Zhengzhou 450052, China; wangzheng@igs-has.cn

* Correspondence: mao@sio.org.cn

Abstract: This study focuses on deriving the total absorption coefficients based on field measurements and satellite data. An extended quasi–analytical algorithm (QAA–GRI) was developed based on the two in situ datasets collected from inland waters of Lake Qiandaohu (QDH) and oceanic waters of the East China Sea (ECS). The key model between absorption coefficients at 510 nm ($a(510)$) and green red index (GRI) was established using power function in the extended QAA–GRI algorithm. The results reveal that the extended QAA–GRI algorithm performs better than the original quasi–analytical algorithm (QAA–v5) and Garver–Siegel–Maritorena’s algorithm (GSM), and the red–green quasi–analytical algorithm (QAA–RGR), at least for the two in situ datasets from the ECS and QDH. For QAA–GRI, the averaged mean absolute percentage error (MAPE) value of retrieved versus in situ total absorption coefficients is approximately 20%. Subsequently, the extended QAA–GRI algorithm was applied to the OLCI satellite imagery, which is the new successor of MERIS with three specific bands (510, 560, and 620 nm). The implementation of the extended QAA–GRI algorithm on OLCI imagery yielded similar results comparable to that of the QAA–v5 in the ECS region. Furthermore, the application of the algorithm on seasonal and annual MERIS satellite imagery help clarify the combined influences from Yangtze River discharge and coastal currents on the distribution of total absorption in the ECS waters. This study suggests that the extended QAA–GRI algorithm is an alternative for retrieving total absorption coefficient, although it is not recommended for highly turbid waters.

Keywords: absorption coefficient; green–red quasi–analytical algorithm; Lake Qiandaohu and East China Sea; OLCI and MERIS satellite data



Citation: Shi, L.; Mao, Z.; Zhang, Y.; Wang, Z.; Tu, Q. An Extended Quasi–Analytical Algorithm for Retrieving Absorption Coefficient Using 510–620 nm Bands from OLCI and MERIS Satellite Data. *Water* **2024**, *16*, 67. <https://doi.org/10.3390/w16010067>

Academic Editor: Renato Morbidelli

Received: 9 November 2023

Revised: 19 December 2023

Accepted: 20 December 2023

Published: 23 December 2023



Copyright: © 2023 by the authors. Licensee MDPI, Basel, Switzerland. This article is an open access article distributed under the terms and conditions of the Creative Commons Attribution (CC BY) license (<https://creativecommons.org/licenses/by/4.0/>).

1. Introduction

Total absorption coefficients ($a(\lambda)$, λ is wavelength) are a key component of the inherent optical properties (IOPs) of water bodies. They are crucial in aquatic and optical environments and serve as a link between satellite ocean color remote sensing and optically active constituents (OACs). For instance, $a(\lambda)$ is important for the determination of biogeochemical parameters, such as the light distribution above or under water [1–4], chlorophyll–a and total suspended matter concentrations [5,6], water clarity [7], phytoplankton biomass [8], primary production [9], phytoplankton community structure or functional type [10,11], and particulate and dissolved organic carbon [12,13]. Since the above parameters are directly or indirectly determined by absorption coefficients of phytoplankton, non–algal particles (NAP), and chromophoric dissolved organic matter (CDOM). Retrieval of the absorption coefficient using remote sensing has given insight into the biological and biogeochemical process within the water body.

Several algorithms for absorption coefficient retrieval have been developed, ranging in complexity from empirical to semi-analytical approaches [14–20]. Empirical algorithms are achieved by directly relating $a(\lambda)$ and remote sensing reflectance ($R_{rs}(\lambda)$). It is widely known that empirical algorithms are data-driven approaches, based on statistical methods, thus, resulting in limitations when applied to different type of waters [21]. However, semi-analytical algorithms, established mainly on the basis of radiative transfer model, which adopt several parameterized methods to approximate the radiative transfer function in physics [22,23], commonly perform better than empirical algorithms in those waters with large variations in optical properties. Garver and Siegel [24] developed a nonlinear statistical model for the retrieval of the $a(\lambda)$ that presupposes knowledge of the specific spectral absorption coefficient of phytoplankton, NAP , and $CDOM$, as well as the specific backscattering coefficient for particles. Maritorena et al. [25] optimized the former model (called GSM01) to make it more suitable for global ocean color data. Boss et al. [15] developed a constrained linear matrix inversion to estimate absorption and backscattering coefficient, and found that the approach can reduce some uncertainties in the inversion results. Lee et al. [26] proposed a simple-to-implement, high-efficiency multiband quasi-analytical algorithm (QAA), which does not have to pre-define the spectral shape of the absorption coefficients related to OACs. The QAA is a stepwise algorithm with several empirical models, which establishes relations between $R_{rs}(\lambda)$ and $a(\lambda)$ based on radiative transfer equation. It has been proven that the QAA algorithm has great potential for $a(\lambda)$ retrieval compared to empirical algorithms [27,28], and has already been adopted in NASA's software platform (SeaDAS) to process satellite ocean color data. Nevertheless, there are several QAA-based algorithms that have been proposed to improve the key model of $a(\lambda_0)$ (λ_0 , reference band) estimation for diverse waters [19,20,29,30]. Up-to-date, semi-analytical algorithms are still widely used and effective algorithms for $a(\lambda)$ estimation, even though a lot of efforts are required to further validate and refine the performance over different optical water types [31].

Several of the currently used algorithms have been further applied to the ocean color satellite data, i.e., sea-viewing wide field-of-view sensor (SeaWiFS) [32,33], moderate resolution imaging spectroradiometer (MODIS) [20,34], visible infrared imaging radiometer (VIIRS) [35,36], medium resolution imaging spectrometer (MERIS) [37,38], geostationary ocean color imager (GOCI) [39], Landsat series [18,40], etc. However, few studies have taken advantage of the ocean and land color instrument (OLCI) on Sentinel-3A, which is a relatively new ocean color sensor launched in 2016. OLCI offers a higher spectral resolution in the visible and near-infrared wavelengths with high signal than VIIRS. Additionally, OLCI strikes a balance between spatial and spectral resolution with higher signal-to-noise ratio compared to Landsat series or Sentinel 2A/B, which makes it more suitable for extensive water bodies and coastal areas where fine spectral discrimination is needed. Therefore, it is necessary to explore appropriate algorithms to facilitate the application of the OLCI data and further its potential.

In this study, we extended green-red band quasi-analytical algorithm (QAA-GRI) for derivation of total absorption coefficients both from in situ data and OLCI satellite imagery. The QAA-GRI algorithm is enhanced by using a new empirical model between the green red index (GRI) and total absorption coefficient at 510 nm based on two in situ field measurements. By enhancement, the model can be applied to oceanic and inland waters rather than to a single water type in our previous study [30]. The algorithm is further applied to the OLCI and MERIS satellite data, and the temporal and spatial variations in total absorption coefficient were investigated and discussed over the East China Sea (ECS). This study gives preliminary evidence that the extended QAA-GRI has good applicability over oceanic and inland waters, and provides an alternative to OLCI and MERIS satellite data for $a(\lambda)$ inversion.

2. Data and Methods

2.1. Field Measurements

The field measurements were undertaken in Lake Qiandaohu (QDH) during nine cruises from June to December 2015 and from March to May 2016. The trophic level of the water quality of lake QDH is oligotrophic, and has the trend of becoming mesotrophic [41]. A total of 144 water samples were collected, among which a total of 46 stations (Figure 1b) have coincident $a(\lambda)$ and $R_{rs}(\lambda)$. The two field measurements were carried out in the ECS on 1–12 January and 25 May–2 June 2017. In the present study, a total of 127 sampling sites were used during the ECS cruises, among which a number of 47 stations (excluding those sites located in coastal waters with high concentrations in suspended sediments, since the QAA algorithms are not suitable for highly turbid waters [29]) have a full suite of coincident remote sensing reflectance and total absorption coefficients (Figure 1c).

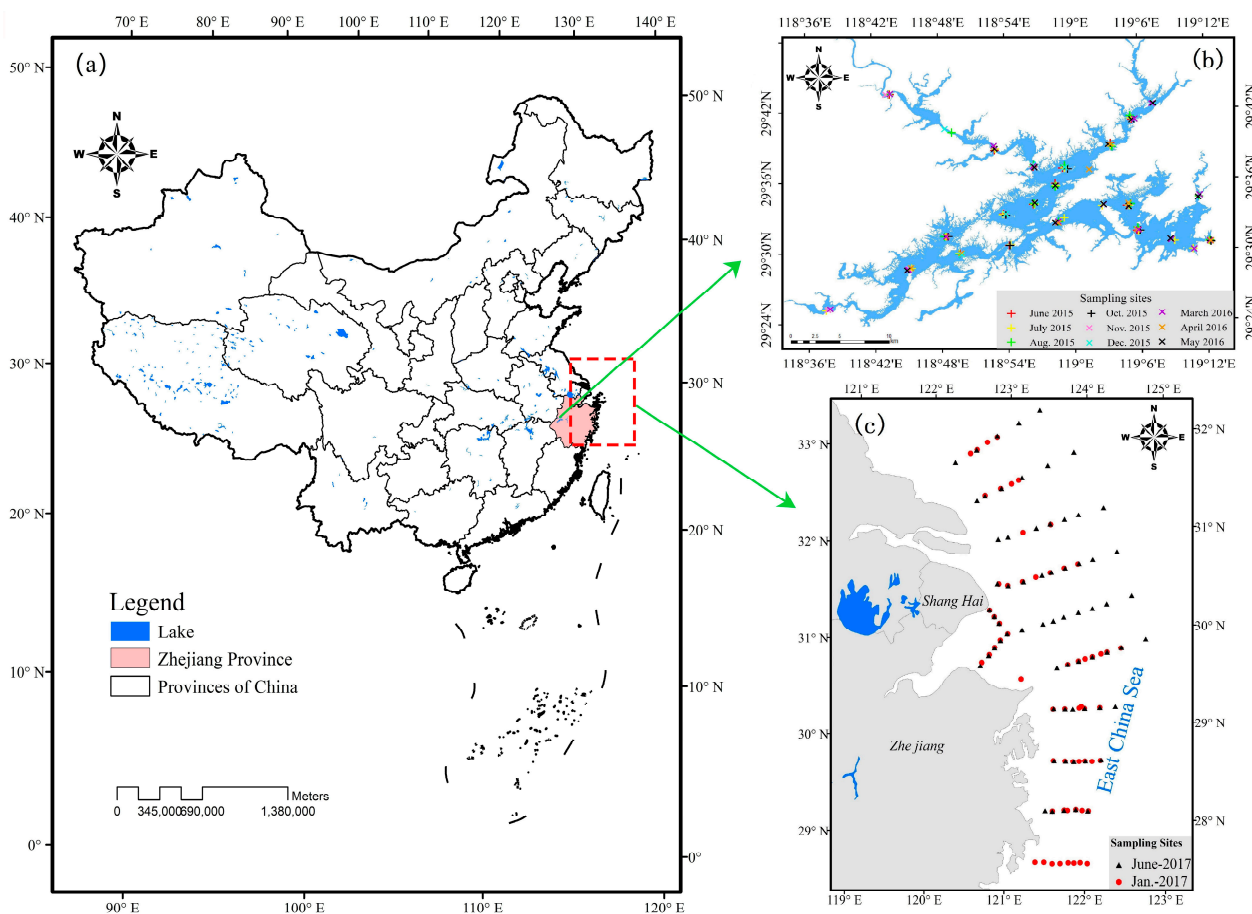


Figure 1. (a) Field sampling sites’ geographical locations; (b) sampling sites in the QDH area, Zhejiang Province; (c) sampling sites in the ECS area.

The remote sensing reflectance was measured using an ASD field spectrometer (Field spec 4), with a spectral range of 350~2500 nm and a spectral resolution of 1.2 nm. The detail method of field measurement can refer to Mueller and Fargion [42]. The $R_{rs}(\lambda)$ was calculated as:

$$R_{rs}(\lambda) = \frac{L_{sw}(\lambda) - rL_{sky}(\lambda)}{\pi L_g(\lambda) / \rho_g(\lambda)} \quad (1)$$

where $L_{sw}(\lambda)$ represents the radiance from the water; $L_{sky}(\lambda)$ stands for diffused sky radiance; r refers to the surface Fresnel reflectance, which is not spectrally constant, and is determined by spectral distribution of skylight and surface wind speed. An average value

of r , 0.026, was adopted in this study according to Cui et al. [43]; $L_g(\lambda)$ and $\rho_g(\lambda)$ stands for the radiance and reflectance from the Spectralon plaque, respectively.

Measurements of the absorption coefficient of CDOM ($a_{CDOM}(\lambda)$) were performed in the laboratory according to the ocean optical protocols [42], and were detailed in our previous study [30]. Briefly, CDOM samples were filtered with a pore size of 0.22 μm , then absorbance of the filtered water was measured over 250~860 nm at 1 nm increments using a Perkin Elmer (PE) lambda-35 spectrophotometer. The absorption coefficient of phytoplankton ($a_{ph}(\lambda)$) and non-algal particle ($a_{NAP}(\lambda)$), were determined according to the quantitative filter technique [44], calculated from their absorbance measured at 1 nm increments from 300~800 nm using a PE lambda-950 spectrophotometer. Consequently, $a(\lambda)$, can be calculated as [45]:

$$a(\lambda) = a_w(\lambda) + a_{ph}(\lambda) + a_{NAP}(\lambda) + a_{CDOM}(\lambda) \tag{2}$$

where $a_w(\lambda)$ is the pure water absorption coefficients reported by Pope and Fry [46].

2.2. OLCI and MERIS Satellite Data

The Sentinel-3 OLCI, launched in February 2016, is a successor of the ENVISAT MERIS instrument. The OLCI is suitable for retrieving parameters of water quality in oceanic, coastal, and inland waters, with 21 spectral bands spanning from 400 to 1020 nm, coverage at 300 m full resolution, high signal-to-noise ratio, and reduced sun glint compared to the MERIS. Note that OLCI or MERIS have specific bands that differ from the other commonly used ocean color sensors in the range of 560~620 nm (Figure 2). Specially, none of the present algorithms have used the 620 nm band for IOPs retrieval.

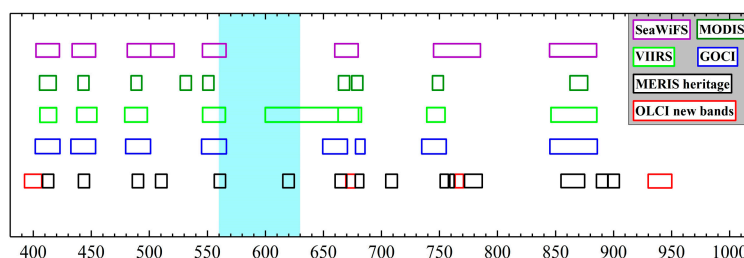


Figure 2. Spectral bands (location and width) of commonly used ocean color sensors, including SeaWiFS, MODIS, VIIRS, GOCI, MERIS, and OLCI. Among these sensors, only MERIS and OLCI have spectral bands located between 560 and 630 nm (cyan background).

In this study, the OLCI level-2B WFR product acquired from the European Space Agency (ESA) Copernicus Open Access Hub (<https://scihub.copernicus.eu/>, 1 November 2023) was chosen as a representative demonstration to exhibit the performance of the extended QAA-GRI algorithm. The OLCI Level-2B data involve atmospheric corrections, as well as the retrieval of ocean color parameters related to oceans. These corrections aim to mitigate the impact of atmospheric interference and other factors, ensuring that the resulting data are more accurate and suitable for scientific analysis. Two Sentinel-3 OLCI level 2B WFR images covering ECS with less cloud captured on 21 May 2019 were chosen for demonstration. The satellite images were joined together using mosaic technology, and the pixels of highly turbid waters and atmospheric correction failed were masked out. In addition, the seasonal and annually composite MERIS level 3 products acquired from the NASA website (<http://oceancolor.gsfc.nasa.gov>, 1 November 2023) were used for investigating the temporal-spatial dynamics of total absorption coefficients by QAA-GRI over the ECS. The level 3 processing involves aggregating and summarizing the level 2 data, providing spatial and temporal averages, and generating products suitable for global scale. Satellite data preprocessing including stitching, masking, and cropping is carried out in the SNAP software, which is an open-source software developed by the ESA for the analysis and visualization of satellite data.

2.3. Accuracy Statistics

To evaluate the performance of the extended algorithm, determination coefficients (R^2), the root mean square error (RMSE), and the mean absolute percentage error (MAPE), are used in this study. They are defined as follows:

$$RMSE = \sqrt{\frac{\sum_{i=1}^n (a_{estimated,i} - a_{in_situ,i})^2}{n}} \quad (3)$$

$$MAPE = \left(\sum \frac{|a_{estimated,i} - a_{in_situ,i}|}{a_{in_situ,i}} / n \right) \times 100\% \quad (4)$$

where n is the number of observations. $a_{in_situ,i}$ and $a_{estimated,i}$ are the in situ and retrieved absorption coefficient at each station i , respectively.

3. Results

3.1. Optical Variability of the ECS and QDH Datasets

Figure 3a,c depicts the variation in R_{rs} measured in the ECS and QDH. The R_{rs} measured in QDH show a typical characteristic of oligotrophic inland waters, the magnitude of which is small, ranging from 0 to 0.015 sr^{-1} , indicating the relatively clean water body of QDH. The majority of R_{rs} in the ECS have a magnitude ranging from 0 to 0.038 sr^{-1} , which is significantly higher than that of the QDH. Moreover, there are a few R_{rs} mainly distributing in near-shore waters, where R_{rs} have a high magnitude, especially in the red and near-infrared red wavelengths. The spectra of $a_{pc}(\lambda)$, which represent the sum of $a_p(\lambda)$ and $a_{CDOM}(\lambda)$ of ECS and QDH, are shown in Figure 3b,d, respectively. The spectral slope of $a_{pc}(\lambda)$ before 500 nm in QDH is higher than that in ECS, which suggests CDOM dominate waters of QDH. In addition, the difference in $a_{pc}(\lambda)$ between 560 and 620 nm is smaller than that of $a_w(\lambda)$. The characteristic of $R_{rs}(\lambda)$ and $a_{pc}(\lambda)$ indicates that the rapid decrease in R_{rs} from 560 to 620 nm is primarily caused by strong absorption of pure water, rather than by particles and CDOM in ECS and QDH.

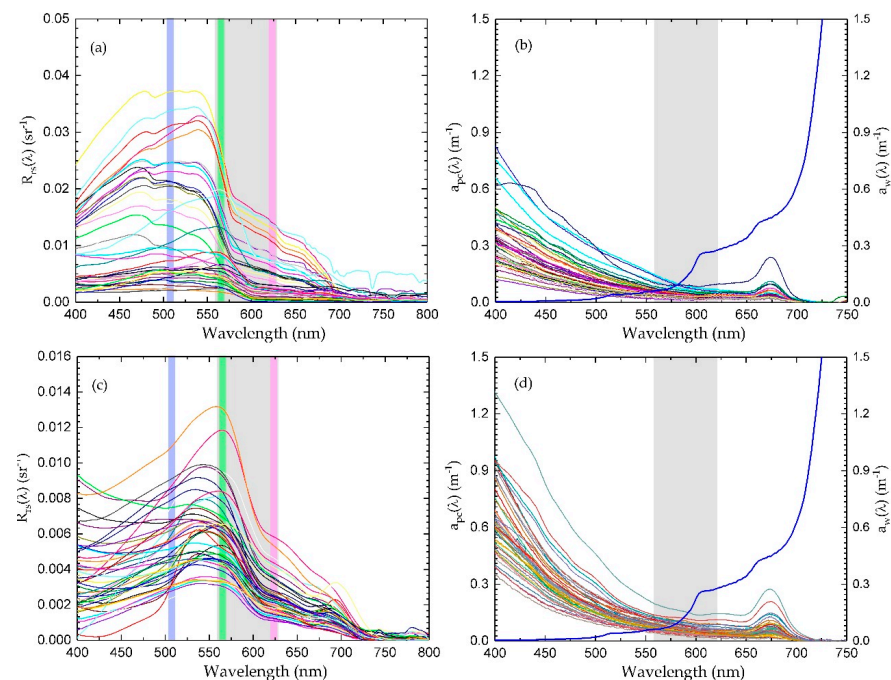


Figure 3. (a–c) R_{rs} spectra for ECS and QDH, respectively; (b–d) a_{pc} spectra measured in the ECS and QDH, respectively (thick blue line represents a_w).

Since the extended algorithm was developed using the ECS and QDH datasets in this study, it is essential to analyze their optical variability to better understand where the algorithm may be inapplicable when applied to different types of waters. Figure 4a shows the ternary plot of different absorbing components at 443 nm. It clearly signifies that the majority of the in situ data belong to phytoplankton or CDOM-dominated waters, and the contribution of non-algal particles among the three components does not exceed 0.4. In particular, QDH is mainly characterized as a low-chlorophyll, CDOM-dominated water system.

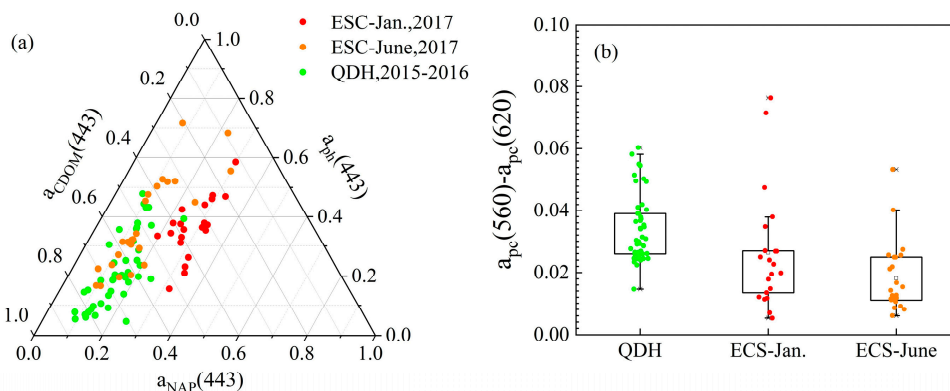


Figure 4. (a) Ternary plot of the ECS and QDH datasets, which illustrates the relative contribution of a_{NAP} , a_{ph} , and a_{CDOM} at 443 nm; (b) box plot shows the statistics of $a_{pc}(560) - a_{pc}(620)$ in the ECS and QDH.

Figure 4b exhibits the statistical results of $a_{pc}(560) - a_{pc}(620)$ among the two datasets. It is a clear demonstration of the fact that the value of $a_{pc}(560) - a_{pc}(620)$ is far less than the value of $a_w(560) - a_w(620)$ (0.213 m^{-1}), which implies that certain conditions have been met to establish the relation between GRI and $a(510)$ proposed in our previous study [30].

3.2. Enhancement of QAA–GRI Algorithm

From the above analysis, the original QAA–GRI algorithm proposed in our previous study [30] can be extended to be applied to the two in situ datasets by improving the model between green–red index (GRI, see Table 1 step 2 in this study) and $a(510)$.

Table 1. An extended QAA–GRI for retrieving total absorption coefficient, step 2 was established in this study, other steps are based on QAA.

Steps	Property	Derivation	Methods
0	r_{rs}	$= R_{rs} / (0.52 + 1.7R_{rs})$	Semi-analytical
1	$u(\lambda)$	$= \frac{-0.089 + \sqrt{0.089^2 + 4 \times 0.125 r_{rs}}}{2 \times 0.125}$	Semi-analytical
2	$a(\lambda_0)\lambda_0 = 510 \text{ nm}$	$GRI = 0.213 \times \frac{R_{rs}(560) \times R_{rs}(620)}{R_{rs}(560) - R_{rs}(620)} \times \frac{1}{R_{rs}(510)}$ $= 0.4654 \times GRI^{0.55}$	Semi-analytical
3	$b_{bp}(\lambda_0)$	$= \frac{u(\lambda_0)a(\lambda_0)}{1 - u(\lambda_0)} - b_{bw}(\lambda_0)$	Analytical
4	Y	$= 2.8 \left[1 - 1.2 \exp(-0.9 \frac{r_{rs}(443)}{r_{rs}(\lambda_0)}) \right]$	Empirical
5	$b_{bp}(\lambda)$	$= b(\lambda_0) \left(\frac{\lambda_0}{\lambda} \right)^Y$	Semi-analytical
6	$a(\lambda)$	$= \frac{(1 - u(\lambda))(b_{bw}(\lambda) + b_{bp}(\lambda))}{u(\lambda)}$	Analytical

As shown in Figure 5, there is a good relationship between GRI and $a(510)$, which can be expressed as Equation (5) using a power–fitted method for the QDH and ECS datasets.

$$a(510) = 0.4654 \cdot GRI^{0.55} \quad (5)$$

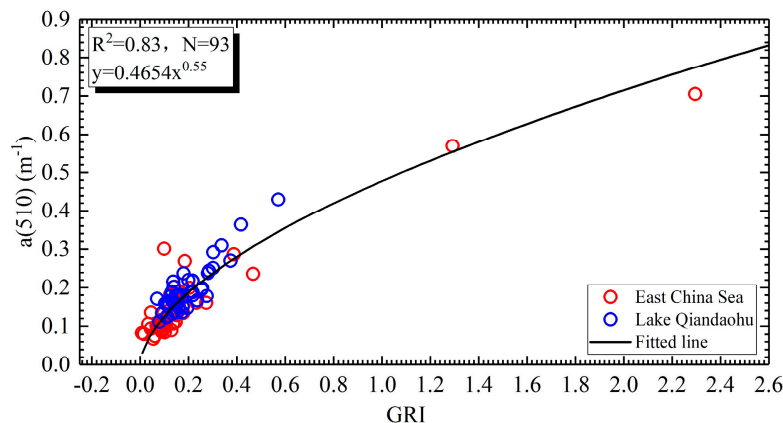


Figure 5. Relationship between the GRI and absorption coefficient at reference band 510 nm using in situ data of the ECS and QDH.

Once the key model was established, the QAA– GRI can be extended to broader application for retrieving $a(\lambda)$ follow the procedure of QAA, as shown in Table 1.

3.3. Performance of the Extended QAA– GRI for the In Situ Datasets

A comparison of the GSM and QAA– GRI algorithms is exhibited in Figure 6 when applied to the ECS. Both the GSM and QAA– GRI show good performance of $a(\lambda)$ at different bands. However, QAA– GRI performs significantly better than the GSM, at least for this ECS dataset. The mean R^2 values between the retrieved and in situ $a(\lambda)$ for GSM and QAA– GRI at 443, 490, and 510 nm are 0.33 and 0.88, respectively, and the mean MAPE values are 56% and 21%, respectively. Furthermore, the performance of the extended QAA– GRI algorithm in retrieving $a(\lambda)$ is compared to other QAA–based algorithms that can be applied in the ECS waters. A comparison of the retrieved and in situ $a(\lambda)$ at 443, 490, 510, 560, and 620 nm for the different algorithms is presented in Figure 7, since these specific bands are typically characteristic bands in ocean color remote sensing [26]. Overall, the data points of the three algorithms that are derived versus in situ $a(\lambda)$ are approximately concentrated on the 1:1 line for the ECS dataset. However, the QAA– GRI performs slightly better than QAA– $v5$ and QAA– RGR . This result can be attributed to the fact that QAA– GRI jointly uses band ratio and band difference approaches, which is less sensitive to uncertainties in $R_{rs}(\lambda)$ than the single–band ratio method used in QAA– $v5$ and QAA– RGR [46].

Figure 8 shows a comparison of retrieved versus in situ $a(\lambda)$ for the QAA– GRI and GSM algorithms in inland water of QDH. Intuitively, the data points of QAA– GRI derived versus in situ $a(\lambda)$ are much closer to the 1:1 line, whereas the GSM performs a slight underestimation. The mean R^2 value between the retrieved and in situ $a(\lambda)$ at 443, 490, and 510 nm is 0.46 and 0.67 for GSM and QAA– GRI , respectively, and the mean MAPE is 34.8% and 17.8%, respectively. This indicates that QAA– GRI performs better than the GSM in $a(\lambda)$ retrievals, at least for the QDH. The comparison performance of QAA– $V5$, QAA– RGR , and QAA– GRI is presented in Figure 9. It shows that the data point retrievals of $a(\lambda)$ by the three algorithms are approximately centralized near the 1:1 line. However, the results retrieved by QAA– $v5$ are slightly less accurate than that by QAA– RGR , whereas the retrievals by QAA– RGR tend to be underestimated compared to QAA– GRI .

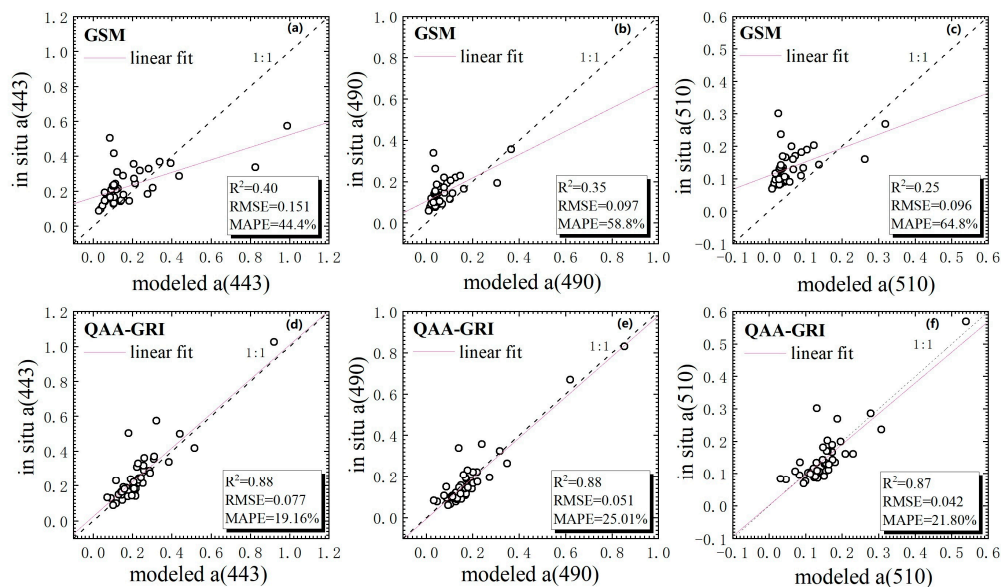


Figure 6. Comparison of the (a–c) GSM, and (d–f) QAA–GRI algorithms derived and in situ $a(\lambda)$ for the ECS dataset at 443, 490, and 510 nm, respectively.

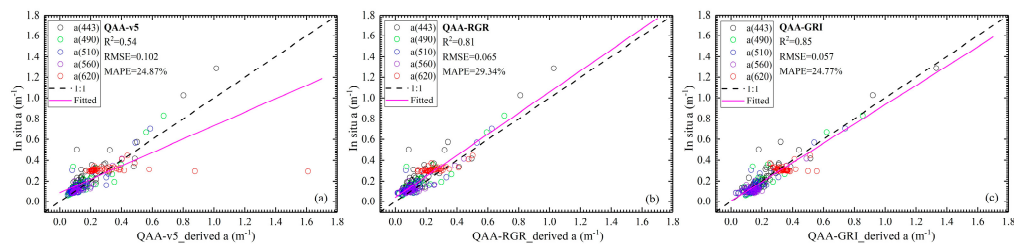


Figure 7. Comparison of the (a) QAA–v5, (b) QAA–RGR, and (c) QAA–GRI derived and in situ $a(\lambda)$ for ECS dataset at 443, 490, 510, 560, and 620 nm.

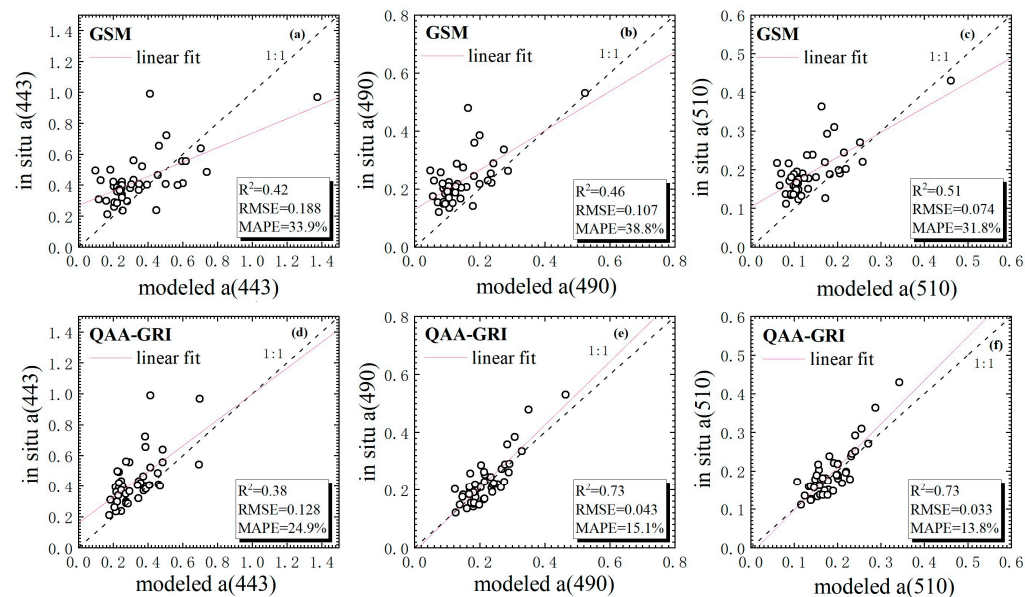


Figure 8. Comparison of the (a–c) GSM and (d–f) QAA–GRI derived and in situ $a(\lambda)$ for the QDH dataset at 443, 490, and 510 nm, respectively.

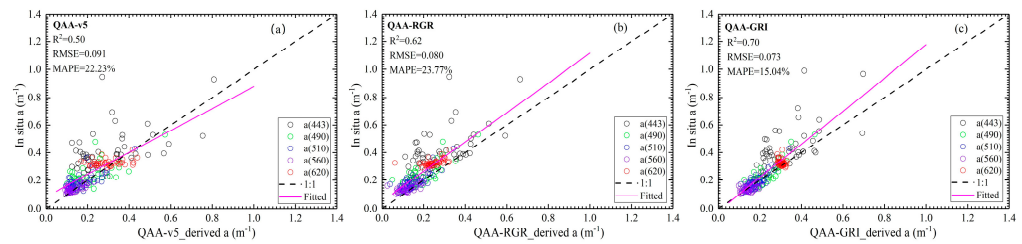


Figure 9. Comparison of the (a) QAA–v5, (b) QAA–RGR, and (c) QAA–GRI algorithms derived and in situ $a(\lambda)$ for the QDH data set at 443, 490, 510, 560, and 620 nm.

4. Discussion

4.1. Application to OLCI Satellite Data

Satellite ocean color data have already been proven to be capable of detecting the magnitude of water color parameters and its spatial and temporal variability. Figure 10 shows the results of $a(443)$ derived from OLCI using QAA–v5 and QAA–GRI. The distribution patterns and spatial gradients of the total absorption coefficient over the ECS region are exhibited. It can be clearly seen that values of $a(443)$ are higher in the nearshore waters than the offshore. The high $a(443)$ values are generally distributed in the mouth of Hangzhou Bay and coastal waters along Zhejiang Province, which indicates the joint effects from the river discharge and coastal currents over the ECS. The decreases in $a(443)$ values offshore indicates that the highly absorbed waters quickly subside in the nearshore region. It should be noted that $a(443)$ values located in the areas highlighted with black boxes (Figure 10a,b) are significantly higher than surrounding ones. This is due to the high chlorophyll–a concentration, which also implies that an algal bloom occurs in this region. The comparison of $a(443)$ retrieved from QAA–v5 and QAA–GRI shows some differences in magnitude. Quantitatively, a histogram of the two $a(443)$ image is given in Figure 10c. It shows that QAA–v5 $a(443)$ is slightly overestimated in the high value domain, and underestimated in the low value domain over the ECS, compared to QAA–GRI, which is consistent with the study of Chen et al. [47]. The standard deviation (Stdev = 0.101) and variation coefficient (CV = 0.848) of the QAA–GRI $a(510)$ image is less than the QAA–v5 $a(443)$ image. This gives some evidence that the QAA–GRI can partly minimize the uncertainty of satellite R_{rs} data.

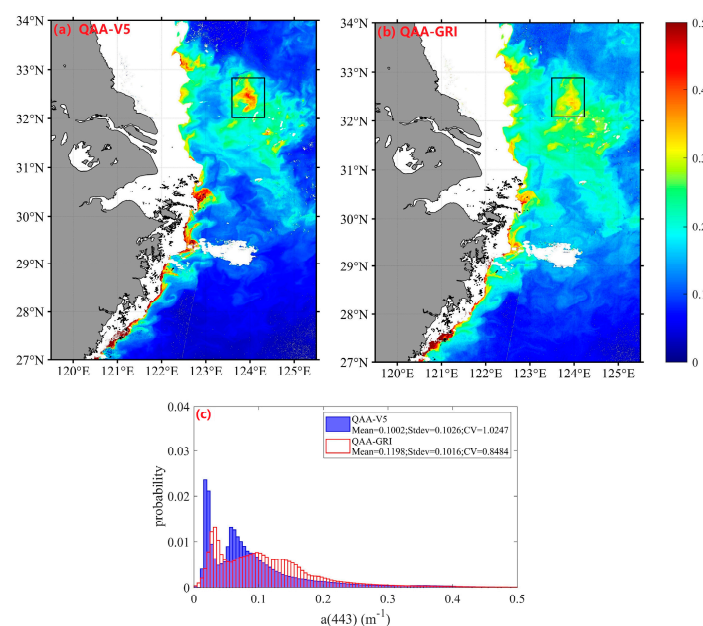


Figure 10. (a,b) Distribution of retrieved $a(443)$ image from QAA–v5 and extended QAA–GRI algorithms; (c) histogram of QAA–v5 and QAA–GRI retrieved $a(443)$ image.

4.2. Seasonal and Annual Variability in ECS Using MERIS Imagery

There are ways to better understand the biogeochemistry of oceanic and coastal systems from satellite remote sensing. In this study, taking the year 2010 as example, the seasonal average climatology of $a(443)$ derived from monthly composite MERIS R_{rs} data is shown in Figure 11. The seasonal distribution demonstrates the significant spatial-temporal variations in $a(443)$ over the ECS region. The averages for $a(443)$ are high along the Yangtze River plume (YRP), Hangzhou Bay mouth (HBM), and nearshore waters during all seasons. However, during winter, the high $a(443)$ area is larger than the other seasons due to the sediment resuspension by strong mixing. Meanwhile, the high values appear near the Yangtze River mouth towards the southeast with an apparent “tongue-shaped” structure. This typical structure is the result of interaction by the Yangtze River diluted water, the Taiwan current, and the offshore current along Zhejiang and Jiangsu provinces. During spring, the high $a(443)$ tongue-shaped structure extends toward the northeast, and becomes unclear compared to that of winter due to the increase in $a(443)$ variation in the surrounding regions. During summer, the tongue-shaped structure becomes small and extended toward the northeast, reaching Jeju Island. During autumn, the tongue-shaped structure changes direction from northwestward to southeastward. These remote sensing patterns are generally consistent with the results reported by Yamaguchi et al. [48] and Sun et al. [49].

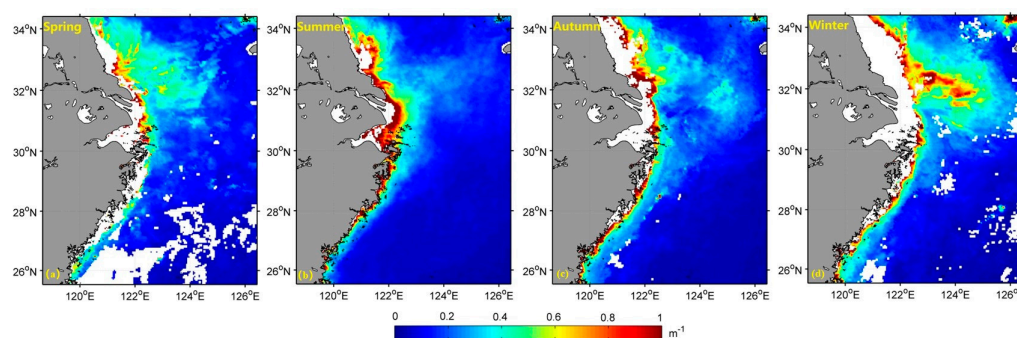


Figure 11. (a–d) MERIS–derived satellite images of climatological seasonal average $a(443)$ over ECS by the extended QAA–GRI algorithm.

Moreover, the annual average climatology of $a(443)$ derived from MERIS from 2002 to 2012 is shown in Figure 12. It shows the annual average $a(443)$ retrieved from MERIS during the past 11 years. The spatial distribution patterns of annual $a(443)$ image for all years are generally similar, with high values in the YRP, HBM, and nearshore coastal waters. Note that tongue-shaped structure extending toward the southeast is quite clear in each year. All the images (Figures 11 and 12) intuitively highlight the combined influences from Yangtze River discharge and ocean currents on the distribution of total absorption in the ECS waters.

4.3. Uncertainty in Application of the Extended Algorithm

The extended QAA–GRI is established upon the original QAA, so the uncertainty will propagate to the next step in the step–by–step procedure. One of the uncertainties is the remote sensing reflectance, since the above–water method for $R_{rs}(\lambda)$ measurement can be influenced by various factors, such as the viewing angle, whitecaps and clouds, skylight, and sun glint. Additionally, the laboratory analysis might also introduce uncertainty, such as the ‘inner filter effect’ of CDOM measurements [50]. Furthermore, the QAA–GRI has the same limitations with QAA when applied to the highly turbid waters. As presented in Figure 4 and Equation (5), it demonstrates a good performance in the estimation of $a(510)$ when using the two in situ datasets. However, it is worth noting that Equation (5) might exhibit some uncertainties in the high Y –value region (Figure 4), due to the scarcity of data points in this region. Moreover, this reliable relation between $a(510)$ and GRI might be

invalid in those waters where the optical properties are dominated by suspended sediment with high concentration. Therefore, the QAA–GRI is recommended to be used in those phytoplankton– or CDOM–dominated waters, both in inland and oceanic environments, and it may have a better performance compared to the QAA.

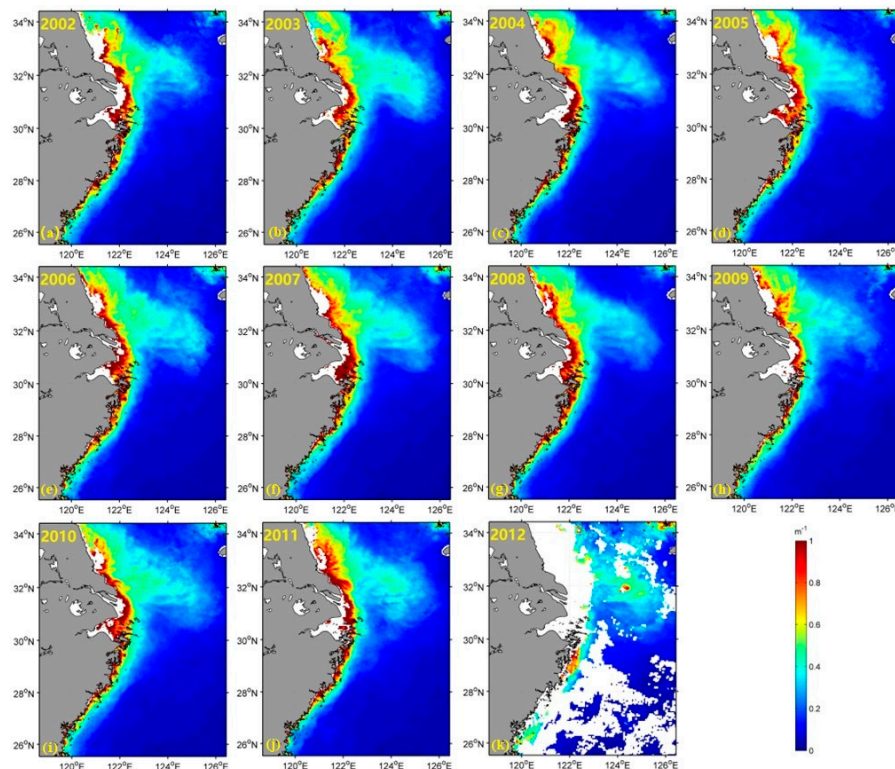


Figure 12. (a–k) Distribution of climatological annually average $a(443)$ derived from MERIS data by the extended QAA–GRI algorithm.

Our study shows a preliminary capacity to retrieve absorption coefficients for monitoring oceanic waters in the ECS using the OLCI and MERIS satellite imagery. The results imply that they can provide valuable information on absorption coefficients, and possess certain potential in phytoplankton bloom via absorption coefficient retrieval at the appropriate spatiotemporal scales both in inland and oceanic waters. However, it is worth noting that the QAA–GRI might yield an underestimated result in relatively turbid coastal waters using MERIS and OLCI satellite data. Additionally, the interference factors of QAA–GRI used in MERIS and OLCI satellite imagery is the accuracy of atmospheric correction, since the atmospheric correction method for case one waters may result in significant errors when applied to inland waters.

5. Conclusions

Total absorption coefficient is one of the key parameters of IOPs for quantitative retrieval in ocean color remote sensing. The QAA–GRI algorithm was successfully extended to both oceanic and inland waters. An encouraging performance was achieved when the extended algorithm was calibrated using the two independent in situ QDH and ECS datasets. QAA–GRI shows an advantage in retrieving absorption coefficient compared to the GSM, QAA–v5, and QAA–RGR algorithms. We further adopted the extended QAA–GRI algorithm for the Sentinel–3 OLCI satellite data covering the ECS region, and found that it not only generated reasonable results but also improved the retrieval of total absorption coefficient in ECS waters compared to the QAA–v5 algorithm. In addition, the extended QAA–GRI algorithm is also applied to the MERIS composited products, and results show clear seasonal and annual variations in total absorption coefficient resulting from the com-

bined effects of hydrodynamic and ecological factors in the ECS region. This study shows the potential of retrievals of various ocean color parameters of interest (i.e., absorption coefficient of *CDOM*, *NAP*, and phytoplankton; backscattering coefficients, etc.) by using OLCI satellite data, although the QAA–GRI algorithm is not recommended to be used in those highly turbid waters. Further refinements and testing might be necessary to confirm its reliability before applying the QAA–GRI to other complex aquatic environments.

Author Contributions: Conceptualization, L.S. and Z.M.; methodology, L.S.; data curation, Z.M. and L.S.; formal analysis and visualization, L.S. and Z.W.; investigation, L.S., Z.W. and Y.Z.; writing—original draft, L.S.; writing—review and editing, Y.Z. and Q.T.; All authors have read and agreed to the published version of the manuscript.

Funding: This work was funded in part by Zhejiang Provincial Natural Science Foundation of China under Grant No. LQ21D060002, in part by National Natural Science Foundation of China (42006160), in part funded by a Project Supported by Scientific Research Fund of Zhejiang Provincial Education Department (Y202045296), and in part by Key Laboratory for Technology in Rural Water Management of Zhejiang Province, Zhejiang University of Water Resources and Electric Power.

Acknowledgments: MERIS and OLCI satellite data were obtained from the European Space Agency (ESA) through the Copernicus Open Access Hub. We thank the staff of the Second institute of Oceanography for their support in the laboratory. We also thank the anonymous reviewers for their useful and conscientious comments on the manuscript.

Conflicts of Interest: The authors declare no conflict of interest.

References

- Gordon, H.R.; Brown, O.B.; Jacobs, M.M. Computed Relationships Between the Inherent and Apparent Optical Properties of a Flat Homogeneous Ocean. *Appl. Opt.* **1975**, *14*, 417. [[CrossRef](#)] [[PubMed](#)]
- Morel, A. In—Water and Remote Measurements of Ocean Color. *Bound.—Layer Meteorol.* **1980**, *18*, 177–201. [[CrossRef](#)]
- Loisel, H.; Stramski, D. Estimation of the Inherent Optical Properties of Natural Waters from the Irradiance Attenuation Coefficient and Reflectance in the Presence of Raman Scattering. *Appl. Opt.* **2000**, *39*, 3001. [[CrossRef](#)] [[PubMed](#)]
- Lee, Z.P.; Darecki, M.; Carder, K.L.; Davis, C.O.; Stramski, D.; Rhea, W.J. Diffuse Attenuation Coefficient of Downwelling Irradiance: An Evaluation of Remote Sensing Methods. *J. Geophys. Res. Oceans* **2005**, *110*(C2). [[CrossRef](#)]
- Bricaud, A.; Stramski, D. Spectral Absorption Coefficients of Living Phytoplankton and Nonalgal Biogenous Matter: A Comparison Between the Peru Upwelling Area and the Sargasso Sea. *Limnol. Oceanogr.* **1990**, *35*, 562–582. [[CrossRef](#)]
- Bricaud, A.; Morel, A.; Babin, M.; Allali, K.; Claustre, H. Variations of Light Absorption by Suspended Particles with Chlorophyll a Concentration in Oceanic (Case 1) Waters: Analysis and Implications for Bio–Optical Models. *J. Geophys. Res.* **1998**, *103*, 31033–31044. [[CrossRef](#)]
- Lee, Z.; Shang, S.; Qi, L.; Yan, J.; Lin, G. A Semi–Analytical Scheme to Estimate Secchi–Disk Depth from Landsat–8 Measurements. *Remote Sens. Environ.* **2016**, *177*, 101–106. [[CrossRef](#)]
- Lyon, P.E.; Hoge, F.E.; Wright, C.W.; Swift, R.N.; Yungel, J.K. Chlorophyll Biomass in the Global Oceans: Satellite Retrieval Using Inherent Optical Properties. *Appl. Opt.* **2004**, *43*, 5886–5892. [[CrossRef](#)]
- Tilstone, G.H.; Smyth, T.J.; Gowen, R.J.; Martinez–Vicente, V.; Groom, S.B. Inherent Optical Properties of the Irish Sea and Their Effect on Satellite Primary Production Algorithms. *J. Plankton Res.* **2005**, *27*, 1127–1148. [[CrossRef](#)]
- Ciotti, Á.M.; Cullen, J.J.; Lewis, M.R. A Semi–analytical Model of the Influence of Phytoplankton Community Structure on the Relationship between Light Attenuation and Ocean Color. *J. Geophys. Res. Oceans* **1999**, *104*, 1559–1578. [[CrossRef](#)]
- Kostadinov, T.S.; Cabré, A.; Vedantham, H.; Marinov, I.; Bracher, A.; Brewin, R.J.W.; Bricaud, A.; Hirata, T.; Hirawake, T.; Hardman–Mountford, N.J.; et al. Inter–Comparison of Phytoplankton Functional Type Phenology Metrics Derived from Ocean Color Algorithms and Earth System Models. *Remote Sens. Environ.* **2017**, *190*, 162–177. [[CrossRef](#)]
- Stramski, D.; Reynolds, R.A.; Kahru, M.; Mitchell, B.G. Estimation of Particulate Organic Carbon in the Ocean from Satellite Remote Sensing. *Science* **1999**, *285*, 239–242. [[CrossRef](#)] [[PubMed](#)]
- Cao, F.; Tzortziou, M.; Hu, C.; Mannino, A.; Fichot, C.G.; Del Vecchio, R.; Najjar, R.G.; Novak, M. Remote Sensing Retrievals of Colored Dissolved Organic Matter and Dissolved Organic Carbon Dynamics in North American Estuaries and Their Margins. *Remote Sens. Environ.* **2018**, *205*, 151–165. [[CrossRef](#)]
- Gordon, H.R.; Boynton, G.C. Radiance–Irradiance Inversion Algorithm for Estimating the Absorption and Backscattering Coefficients of Natural Waters: Vertically Stratified Water Bodies. *Appl. Opt.* **1998**, *37*, 3886. [[CrossRef](#)] [[PubMed](#)]
- Boss, E.; Roesler, C. Over Constrained Linear Matrix Inversion with Statistical Selection. Remote Sensing of Inherent Optical Properties: Fundamentals, Tests of Algorithms, and Applications. *IOCCG Rep.* **2006**, *5*, 57–62.

16. Li, S.; Song, K.; Mu, G.; Zhao, Y.; Ma, J.; Ren, J. Evaluation of the Quasi–Analytical Algorithm (QAA) for Estimating Total Absorption Coefficient of Turbid Inland Waters in Northeast China. *IEEE J. Sel. Top Appl. Earth Obs. Remote Sens.* **2016**, *9*, 4022–4036. [[CrossRef](#)]
17. Grunert, B.K.; Mouw, C.B.; Ciochetto, A.B. Deriving Inherent Optical Properties from Decomposition of Hyperspectral Non–Water Absorption. *Remote Sens. Environ.* **2019**, *225*, 193–206. [[CrossRef](#)]
18. Wei, J.; Lee, Z.P.; Shang, S.; Yu, X. Semianalytical Derivation of Phytoplankton, CDOM, and Detritus Absorption Coefficients From the Landsat 8/OLI Reflectance in Coastal Waters. *J. Geophys. Res. Oceans* **2019**, *124*, 3682–3699. [[CrossRef](#)]
19. Yang, W.; Matsushita, B.; Chen, J.; Yoshimura, K.; Fukushima, T. Retrieval of Inherent Optical Properties for Turbid Inland Waters from Remote–Sensing Reflectance. *IEEE Trans. Geos. Remote Sens.* **2013**, *51*, 3761–3773. [[CrossRef](#)]
20. Chen, S.; Zhang, T. Evaluation of a QAA–Based Algorithm Using MODIS Land Bands Data for Retrieval of IOPs in the Eastern China Seas. *Opt. Express* **2015**, *23*, 1908–1925. [[CrossRef](#)]
21. Werdell, P.J.; McKinna, L.I.W.; Boss, E.; Ackleson, S.G.; Craig, S.E.; Gregg, W.W.; Lee, Z.; Maritorea, S.; Roesler, C.S.; Rousseaux, C.S.; et al. An Overview of Approaches and Challenges for Retrieving Marine Inherent Optical Properties from Ocean Color Remote Sensing. *Prog. Oceanogr.* **2018**, *160*, 186–212. [[CrossRef](#)] [[PubMed](#)]
22. Gordon, H.R.; Brown, O.B.; Evans, R.H.; Brown, J.W.; Smith, R.C.; Baker, K.S.; Clark, D.K. A Semianalytic Radiance Model of Ocean Color. *J. Geophys. Res.* **1988**, *93*, 10909–10924. [[CrossRef](#)]
23. Mobley, C.D. Radiative Transfer in the Ocean. In *Encyclopedia of Ocean Sciences*; Academic Press: Cambridge, MA, USA, 2001; pp. 2321–2330. [[CrossRef](#)]
24. Garver, S.A.; Siegel, D.A. Inherent Optical Property Inversion of Ocean Color Spectra and Its Biogeochemical Interpretation: 1. Time Series from the Sargasso Sea. *J. Geophys. Res. Oceans* **1997**, *102*, 18607–18625. [[CrossRef](#)]
25. Maritorea, S.; Siegel, D.A.; Peterson, A.R. Optimization of a Semianalytical Ocean Color Model for Global–Scale Applications. *Appl. Opt.* **2002**, *41*, 2705. [[CrossRef](#)] [[PubMed](#)]
26. Lee, Z.; Carder, K.L.; Arnone, R.A. Deriving Inherent Optical Properties from Water Color: A Multiband Quasi–Analytical Algorithm for Optically Deep Waters. *Appl. Opt.* **2002**, *41*, 5755. [[CrossRef](#)] [[PubMed](#)]
27. Lee, Z.; Arnone, R.; Hu, C.; Werdell, P.J.; Lubac, B. Uncertainties of Optical Parameters and Their Propagations in an Analytical Ocean Color Inversion Algorithm. *Appl. Opt.* **2010**, *49*, 369–381. [[CrossRef](#)] [[PubMed](#)]
28. Li, L.; Li, L.; Song, K.; Li, Y.; Tedesco, L.P.; Shi, K.; Li, Z. An Inversion Model for Deriving Inherent Optical Properties of Inland Waters: Establishment, Validation and Application. *Remote Sens. Environ.* **2013**, *135*, 150–166. [[CrossRef](#)]
29. Le, C.F.; Li, Y.M.; Zha, Y.; Sun, D.; Yin, B. Validation of a Quasi–Analytical Algorithm for Highly Turbid Eutrophic Water of Meiliang Bay in Taihu Lake, China. *IEEE Trans. Geos. Remote Sens.* **2009**, *47*, 2492–2500. [[CrossRef](#)]
30. Shi, L.; Tao, B.; Mao, Z.; Liu, M.; Zhang, Y. Retrieval of Absorption Coefficients for a Drinking Water Source Using a Green–Red Band Quasianalytical Algorithm. *J. Appl. Remote Sens.* **2018**, *12*, 042802. [[CrossRef](#)]
31. Zheng, G.; Stramski, D.; Reynolds, R.A. Evaluation of the Quasi–Analytical Algorithm for Estimating the Inherent Optical Properties of Seawater from Ocean Color: Comparison of Arctic and Lower–Latitude Waters. *Remote Sens. Environ.* **2014**, *155*, 194–209. [[CrossRef](#)]
32. Mélin, F.; Berthon, J.F.; Zibordi, G. Assessment of Apparent and Inherent Optical Properties Derived from SeaWiFS with Field Data. *Remote Sens. Environ.* **2005**, *97*, 540–553. [[CrossRef](#)]
33. Pan, X.; Mannino, A.; Russ, M.E.; Hooker, S.B. Remote Sensing of the Absorption Coefficients and Chlorophyll a Concentration in the United States Southern Middle Atlantic Bight from SeaWiFS and MODIS–Aqua. *J. Geophys. Res. Oceans* **2008**, *113*, 1–15. [[CrossRef](#)]
34. Chu, Q.; Zhang, Y.; Ma, R.; Hu, M.; Jing, Y. MODIS–Based Remote Estimation of Absorption Coefficients of an Inland Turbid Lake in China. *Remote Sens.* **2020**, *12*, 1940. [[CrossRef](#)]
35. Vandermeulen, R.A.; Arnone, R.; Ladner, S.; Martinolich, P. Enhanced Satellite Remote Sensing of Coastal Waters Using Spatially Improved Bio–Optical Products from SNPP–VIIRS. *Remote Sens. Environ.* **2015**, *165*, 53–63. [[CrossRef](#)]
36. Shi, W.; Wang, M.; Zhang, Y. Inherent Optical Properties in Lake Taihu Derived from VIIRS Satellite Observations. *Remote Sens.* **2019**, *11*, 1426. [[CrossRef](#)]
37. Tilstone, G.H.; Peters, S.W.M.; van der Woerd, H.J.; Eleveld, M.A.; Ruddick, K.; Schönfeld, W.; Krasemann, H.; Martinez–Vicente, V.; Blondeau–Patissier, D.; Röttgers, R.; et al. Variability in Specific–Absorption Properties and Their Use in a Semi–Analytical Ocean Colour Algorithm for MERIS in North Sea and Western English Channel Coastal Waters. *Remote Sens. Environ.* **2012**, *118*, 320–338. [[CrossRef](#)]
38. Le, C.; Lehrter, J.C.; Schaeffer, B.A.; Hu, C.; Murrell, M.C.; Hagy, J.D.; Greene, R.M.; Beck, M. Bio–Optical Water Quality Dynamics Observed from MERIS in Pensacola Bay, Florida. *Estuar. Coast Shelf Sci.* **2016**, *173*, 26–38. [[CrossRef](#)]
39. Concha, J.; Mannino, A.; Franz, B.; Kim, W. Uncertainties in the Geostationary Ocean Color Imager (GOCI) Remote Sensing Reflectance for Assessing Diurnal Variability of Biogeochemical Processes. *Remote Sens.* **2019**, *11*, 295. [[CrossRef](#)]
40. Li, J.; Yu, Q.; Tian, Y.Q.; Becker, B.L.; Siqueira, P.; Torbick, N. Spatio–Temporal Variations of CDOM in Shallow Inland Waters from a Semi–Analytical Inversion of Landsat–8. *Remote Sens. Environ.* **2018**, *218*, 189–200. [[CrossRef](#)]
41. Shi, L.; Mao, Z.; Wu, J.; Liu, M.; Zhang, Y.; Wang, Z. Variations in Spectral Absorption Properties of Phytoplankton, Non–Algal Particles and Chromophoric Dissolved Organic Matter in Lake Qiandaohu. *Water* **2017**, *9*, 352. [[CrossRef](#)]

42. Pegau, S.; Zaneveld, J.R.V.; Mitchell, B.G.; Mueller, J.L.; Kahru, M.; Wieland, J.; Stramska, M. Ocean Optics Protocols for Satellite Ocean Color Sensor Validation, Revision 4, Volume IV: Inherent Optical Property Measurement Concepts: Physical Principles and Instruments, Characterizations, Field Measurements and Data Analysis Protocols. In *NASA Technical Memorandum*; NASA: Washington, DC, USA, 2003; Volume IV, pp. 1–76.
43. Cui, T.-W.; Song, Q.-J.; Tang, J.W.; Zhang, J. Spectral Variability of Sea Surface Skylight Reflectance and Its Effect on Ocean Color. *Opt. Express* **2013**, *21*, 24929–24941. [[CrossRef](#)]
44. Tassan, S.; Ferrari, G.M. A Sensitivity Analysis of the “Transmittance—Reflectance” Method for Measuring Light Absorption by Aquatic Particles. *J. Plankton Res.* **2002**, *24*, 757–774. [[CrossRef](#)]
45. Prieur, L.; Sathyendranath, S. An optical classification of coastal and oceanic waters based on the specific spectral absorption curves of phytoplankton pigments, dissolved organic matter, and other particulate materials. *Limnol. Oceanogr.* **1981**, *26*, 671–689. [[CrossRef](#)]
46. Pope, R.M.; Fry, E.S. Absorption Spectrum (380–700 nm) of Pure Water II Integrating Cavity Measurements. *Appl. Opt.* **1997**, *36*, 8710. [[CrossRef](#)]
47. Chen, J.; He, X.; Zhou, B.; Pan, D. Deriving Colored Dissolved Organic Matter Absorption Coefficient from Ocean Color with a Neural Quasi–Analytical Algorithm. *J. Geophys. Res. Oceans* **2017**, *122*, 8543–8556. [[CrossRef](#)]
48. Yamaguchi, H.; Kim, H.C.; Son, Y.B.; Kim, S.W.; Okamura, K.; Kiyomoto, Y.; Ishizaka, J. Seasonal and Summer Interannual Variations of SeaWiFS Chlorophyll a in the Yellow Sea and East China Sea. *Prog. Oceanogr.* **2012**, *105*, 22–29. [[CrossRef](#)]
49. Sun, D.; Huan, Y.; Wang, S.; Qiu, Z.; Ling, Z.; Mao, Z.; He, Y. Remote Sensing of Spatial and Temporal Patterns of Phytoplankton Assemblages in the Bohai Sea, Yellow Sea, and East China Sea. *Water Res.* **2019**, *157*, 119–133. [[CrossRef](#)]
50. Green, S.A.; Blough, N.V. Optical Absorption and Fluorescence Properties of Chromophoric Dissolved Organic Matter in Natural Waters. *Limnol. Oceanogr.* **1994**, *39*, 1903–1916. [[CrossRef](#)]

Disclaimer/Publisher’s Note: The statements, opinions and data contained in all publications are solely those of the individual author(s) and contributor(s) and not of MDPI and/or the editor(s). MDPI and/or the editor(s) disclaim responsibility for any injury to people or property resulting from any ideas, methods, instructions or products referred to in the content.